2023

Solar Sailing Adaptive Control Using Integral Concurrent Learning for Solar Flux Estimation

Luis Enrique Mendoza Zambrano
Embry-Riddle Aeronautical University, mendol10@my.erau.edu

Riccardo Bevilacqua
Embry-Riddle Aeronautical University, bevilacr@erau.edu

Scholarly Commons Citation

Mendoza Zambrano, L. E., & Bevilacqua, R. (2023). Solar Sailing Adaptive Control Using Integral Concurrent Learning for Solar Flux Estimation. *Acta Astronautica, 213*(). https://doi.org/10.1016/j.actaastro.2023.09.025

Solar Sailing Adaptive Control Using Integral Concurrent Learning for Solar Flux Estimation

Luis Enrique Mendoza Zambrano[a], Riccardo Bevilacqua[b,*]

[a] *PhD Student, Aerospace Engineering Department, Embry-Riddle Aeronautical University, 1 Aerospace Blvd LB-256, Daytona Beach, 32114, FL, USA*
[b] *Professor, Aerospace Engineering Department, Embry-Riddle Aeronautical University, 1 Aerospace Blvd LB-262, Daytona Beach, 32114, FL, USA*

Abstract

In the interest of exploiting natural forces for propellant-less spacecraft missions, this investigation proposes an adaptive control strategy to account for unknown parameters in the dynamic modeling of a reflectivity-controlled solar sail spacecraft. A Lyapunov-based control law along with integral concurrent learning is suggested to accomplish and prove global exponential tracking of the estimated parameters and states of interest, without satisfying the common persistence of excitation condition, which in most nonlinear systems cannot be guaranteed a priori. This involves estimating the solar flux or irradiance from the Sun to account for uncertainty and variation over time in this value. To illustrate potential applications, two missions are considered: (1) a geostationary debris removal case and (2) an Earth-Mars interplanetary transfer orbit following a logarithmic spiral reference trajectory. The proposed formulation demonstrates the benefit of estimating the solar flux using integral concurrent learning. Results are compared to trajectories with no estimation to illustrate the need to account for the actual solar flux.

Keywords:

Adaptive Control, Finite Excitation, Integral Concurrent Learning, Solar Irradiance, Solar Sailing.

*Corresponding author. *E-mail address: bevilacr@erau.edu (R. Bevilacqua)*

1. Introduction

In the interest of exploiting natural forces for propellant-less spacecraft missions, numerous solar sail missions are proposed for a wide variety of applications including space exploration, relay communication, technology demonstration missions, *etc* [1]. For instance, the Near-Earth Asteroid (NEA) Scout Mission by NASA, recently onboarded the Space Launch System (SLS), will help determine the physical properties of a near-Earth asteroid using a science-grade camera. The NEA Scout is a CubeSat propelled by a solar sail measuring 925 square feet [2]. In parallel, NASA is developing a new deployable structure known as Advanced Composite Solar Sail System, or *ACS3*, to demonstrate successful sail packing and deployment of composite solar sails within low-Earth orbits (Figure 1) [3]. NASA is also conducting research in diffractive lightsails proposed as a new solar sail concept that would use small gratings embedded in thin films to make a more efficient use of sunlight without sacrificing maneuverability [4]. However, for many solar sail mission applications, active control is required for the stability of a desired orbit. For a solar sail of fixed geometry and characteristic acceleration, active control is unattainable as the only control variables are given by the attitude of the sail [5, 6, 7]. In this context, two proposed solutions to this problem are considered in the literature among which solar flux fluctuations are often neglected. One suggests the implementation of reflectivity modulation technology for orbital control, while the second one assumes a variable-geometry solar sail model [8].

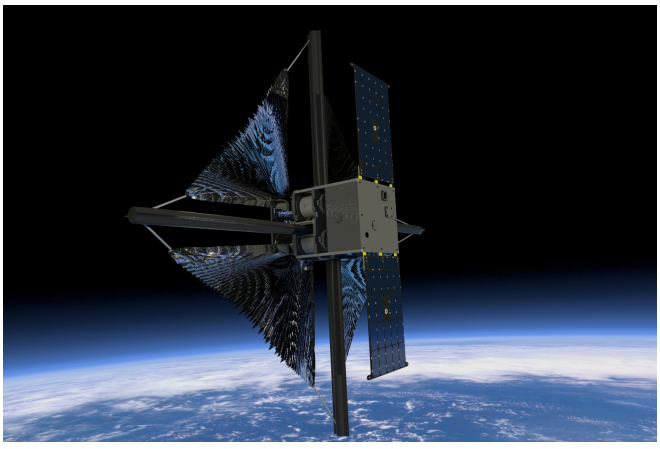

Figure 1: Advanced Composite Solar Sail System *ACS3* concept by NASA [3].

Reflectivity modulation technology is adopted for active control of solar sails in accordance with previous demonstration missions and applications [5, 6, 7, 9]. A reflectivity control device (RCD) is a device manufactured from electrochromic materials composed of a thin layer of polymer dispersed nematic liquid crystals [10]. Effectively, upon application of a low electric voltage, nematic crystals within the film align with the electric field, allowing its reflectivity coefficient to change from a diffusive to a highly specular state [10]. IKAROS (2010), the first successful interplanetary solar sail demonstration mission, employed a reflectivity control device for attitude control [9]. By synchronizing the fraction of switched-on RCDs, the spacecraft was able to change its spinning axis without consuming fuel [11]. RCDs were installed at the periphery of the sail to generate sufficient torque (Figure 2). The trajectory of IKAROS was controlled indirectly by its attitude. IKAROS conveniently performed a reverse turn of its angular momentum vector relative to the inertial frame while approaching Venus as part of its mission [9]. At the present time, a new class of RCDs are under development by the University of Tokyo and JAXA entitled Advanced-RCD or simply A-RCD [10]. Unlike conventional RCDs, A-RCDs deflect the light obliquely to generate a torque perpendicular to the surface of the sail to avoid deformation of the solar sail membrane, also referred to as the windmill effect [10]. An optimal design of the reflection angle at the oblique reflection film is studied in recent literature for future implementation of an additional degree of freedom [10].

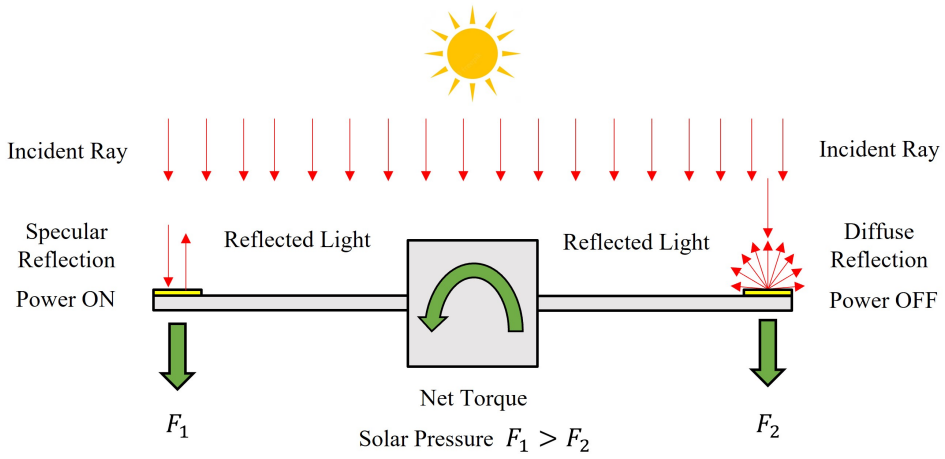

Figure 2: Attitude control concept of the IKAROS mission using RCDs [9].

Substantial research on orbital control has been conducted using RCDs since the introduction of this technology by its pioneer IKAROS. For instance, in Niccolai et al. [5], a full state feedback control law is designed with a linear quadratic regulator (LQR) approach to stabilize an L_1-type artificial equilibrium point using RCDs. Similarly in Mu et al. [6], the application of this technology for solar sail formation flying was investigated for the purpose of tracking a reference trajectory for a magnetosphere mission. Here, the relative solar radiation pressure acceleration was linearized to derive a Lyapunov-based control law followed by a constrained nonlinear predictive controller [6]. It was concluded that small variations in the control variables given by the fraction of switched-on RCDs and the attitude of the spacecraft was sufficient to track a desired orbit [5, 6].

In Gong and Li [12], RCDs are used to stabilize Halo orbits around Lagrange points within the restricted three-body problem. An LQR control policy was compared to a Floquet theory-based control law. In this study, convergence to a family of Halo orbits was accomplished. Similarly, in Biggs and Negri [13], an orbit-attitude control scheme is proposed to track an artificial equilibrium point of the Earth-Moon system. In contrast to Gong and Li [12], RCDs are both used to control the attitude and orbit of the solar sail simultaneously [13]. However, the solar flux was assumed to be a constant and known value.

Recent studies have shown the need to account for solar flux fluctuations [14, 15]. Nevertheless, in most academic papers, solar flux fluctuations are often neglected owing to the assumption of a constant solar radiation pressure coefficient. In addition, it is commonly assumed to be a known parameter. In Vulpetti [14], the effect of the actual solar pressure on low-eccentricity orbits was analyzed using the time series of the Total Solar Irradiance (TSI). Correspondingly, in Vulpetti [15], a heliocentric transfer orbit from Earth to Mars was considered within a large high-precision computer code to study the effect solar flux fluctuations have on the trajectory of a solar sail. The study concluded that solar flux fluctuations as low as $0.1-0.2\%$ of the mean values produce large perturbations on the spacecraft trajectory over the mission time span [15]. To circumvent this problem, a solar flux measurement package has been suggested as part of the attitude and orbital control system. For instance, in Caruso et al. [7], a control law was developed to counteract solar flux fluctuations on the optimal heliocentric transfer of a reflectivity-controlled solar sail assuming real-time measurements of the solar flux are available.

Since 1978, absolute radiometers have been onboarded satellites to measure the solar flux for solar-observation studies [16]. Radiometers onboarded satellites work on the principle of thermal detectors based on heating a black body due to solar radiation absorption [17]. In a vacuum environment, the absorbed radiation that results in a temperature gradient equals the voltage difference in the electrical and optical heating elements. The relationship between these parameters is commonly adjusted via a correction factor to account for uncertainties. More precisely, this also accounts for diffraction losses and the Doppler effect. However, as noted in recent literature, there is no consensus on a single TSI time series as different radiometers measure inconsistent values. In addition, the long-term TSI variability have not been established as most radiometers do not exceed more than a decade due to material degradation [16]. Indeed, accurate solar flux measurements represents a current challenge in the scientific community. The Compact Total Irradiance Monitor-Flight Demonstration (CTIM-FD) mission by NASA is one of the many solar-observation missions in progress that aim to study solar flux variability. The CTIM-FD mission is currently testing future technology for TSI measurements [18]. In addition, the Brazilian Galileo Solar Space Telescope (GSST) aims to study the evolution of the magnetic structure of the Sun as well as its impact to the atmosphere and climate of the Earth based on solar flux measurements [16].

In this sense, a solar flux measurement package, as proposed in the literature to account for solar flux fluctuations, would not be ideal as it would only compromise control capabilities as well as increase the cost of the mission. Alternatively, we suggest an adaptive control scheme along with integral concurrent learning to estimate the irradiance from the Sun. Adaptive control along with concurrent learning (CL) is used to estimate and account for uncertainties and variation over time in unknown parameters without satisfying the common persistence of excitation condition, which for nonlinear systems cannot be guaranteed a priori and is difficult to check online [19]. More precisely, motivated by the desire to increase robustness and improve transient performance, integral concurrent learning (ICL) is suggested as a modified CL formulation with better tracking, in which estimation of the state derivatives are not required [20].

This investigation aims to develop an adaptive control strategy to account for unknown parameters in the dynamic modeling of a reflectivity-controlled solar sail spacecraft. This requires determining the orientation of the spacecraft to achieve a desired maneuver within realistic time compared to optimal control schemes found in literature [7, 21]. A Lyapunov-based control law along with integral concurrent learning is suggested to accomplish and prove global exponential tracking of the estimated parameters and states of interest, without satisfying the common persistence of excitation condition. This involves estimating the solar flux or irradiance from the Sun to account for uncertainty and variation over time in this value. To illustrate applicable applications, two missions are considered in this paper: (1) a geostationary debris removal case and (2) an Earth-Mars interplanetary transfer orbit following a logarithmic spiral reference trajectory. Unlike preliminary research in solar sailing, the results of this paper show a method to estimate the solar flux using integral concurrent learning as well as a stability proof of the nonlinear system to consider. Additionally, a gradient-based control law for the orientation of the sail using Gauss' variational equations is developed to guarantee asymptotic stability for near-Earth maneuvers. Results are compared to trajectories with no estimation to illustrate the need to account for the actual solar flux.

This paper is organized as follows. In Section 2, the dynamic modeling is presented along with the equations of motion of the spacecraft and the optical solar pressure model using RCDs. In Section 3, the Lyapunov-based control design is derived in addition to an integral concurrent learning update law for online estimation of the irradiance from the Sun. In section 4, numerical simulations for two sample missions are considered: (1) a geostationary debris removal case and (2) an Earth-Mars interplanetary transfer orbit following a logarithmic spiral reference trajectory. Finally, remarkable conclusions of this paper are presented in Section 5.

2. Dynamic Modeling

2.1. The Two-Body Equations of Motion

The equations of motion of the spacecraft can be expressed in the Earth-Centered Inertial (ECI) coordinate system given by the following equation. Equivalently, without loss of generality, the Heliocentric Inertial (HCI) reference frame is commonly used for interplanetary missions.

$$\ddot{\boldsymbol{r}} = -\frac{\mu}{r^3}\boldsymbol{r} + \boldsymbol{a}_{srp} + \boldsymbol{a}_d \tag{1}$$

Here, $\boldsymbol{r}$ is the spacecraft position vector and μ is the gravitational parameter of the primary body. $\boldsymbol{a_{srp}}$ is the spacecraft acceleration due to solar radiation pressure while $\boldsymbol{a_d}$ is the disturbance due to other orbital perturbations such as the gravitational effects due to neighboring celestial bodies.

2.2. Classical Orbital Elements

For convenience, the state vector of the spacecraft is expressed in terms of the classical orbital elements $\boldsymbol{q}(t)$: semi-major axis (a), eccentricity (e), inclination (i), right ascension of the ascending node (Ω), argument of periapsis (ω), and true anomaly (υ). Gauss' variational equations (GVEs) provides the time rate of change of the orbital elements as a function of the disturbance acceleration [22], including solar radiation pressure.

$$\frac{da}{dt} = \frac{2}{n\sqrt{1-e^2}}\left[e\sin(\upsilon)P_r + \frac{p}{r}P_s\right] \tag{2a}$$

$$\frac{de}{dt} = \frac{\sqrt{1-e^2}}{na}\left[\sin(\upsilon)P_r + \left(\cos(\upsilon) + \frac{e+\cos(\upsilon)}{1+e\cos(\upsilon)}\right)P_s\right] \tag{2b}$$

$$\frac{di}{dt} = \frac{r\cos(u)}{na^2\sqrt{1-e^2}}P_w \tag{2c}$$

$$\frac{d\Omega}{dt} = \frac{r\sin(u)}{na^2\sin(i)\sqrt{1-e^2}}P_w \tag{2d}$$

$$\frac{d\omega}{dt} = \frac{\sqrt{1-e^2}}{nae}\left[-\cos(\upsilon)P_r + \sin(\upsilon)\left(1+\frac{r}{p}\right)P_s\right] - \frac{r\cot(i)\sin(u)}{h}P_w \tag{2e}$$

$$\frac{d\upsilon}{dt} = \frac{p\cos(\upsilon)}{eh}P_r - (p+r)\sin(\upsilon)P_s + \frac{h}{r^2} \tag{2f}$$

where u is the argument of latitude, h is the magnitude of angular momentum, n is the mean motion, and p is the semi-latus rectum of the orbit. The disturbance acceleration is described in the Local-Vertical-Local-Horizontal (LVLH) coordinate system centered at the center of mass of the spacecraft along the in-track (P_r), cross-track (P_s), and normal components (P_w).

2.3. Optical Solar Pressure Model

For the purpose of this research, the following model, adopted from Reference [1] and modified a posteriori in Reference [7] with reflectivity modulation technology, features RCDs for active control of a solar sail considering the optical solar pressure model (Figure 3).

$$\boldsymbol{a}_{srp} = \frac{V P_{srp} A_{tot} \cos\left(\phi_{inc}\right)}{m} \left(\frac{\mathrm{AU}}{r_{\odot}}\right)^2 \left[b_1 \hat{\boldsymbol{e}}_{\odot} + \left(b_2 \cos\left(\phi_{inc}\right) + b_3\right) \hat{\boldsymbol{n}}\right] \tag{3}$$

where m is the mass of the spacecraft, P_{srp} is the local time-varying solar radiation pressure coefficient at a distance of 1 AU, $\hat{\boldsymbol{e}}_{\odot}$ is the position unit vector of the Sun, V is the shadow coefficient given by the conical shadow model [22], ϕ_{inc} is the incidence angle of the sail, $r_{\odot}$ is the Sun-sail distance, and $\hat{\boldsymbol{n}}$ is the surface unit normal vector opposite to the Sun (Figure 3). $\{b_1, b_2, b_3\}$ are the dimensionless force coefficients defined in terms of the thermo-optical film properties.

$$b_1 = 1 - \tilde{r} s \tag{4a}$$

$$b_2 = 2 \tilde{r} s \tag{4b}$$

$$b_3 = B_f \tilde{r} (1 - s) + (1 - \tilde{r}) \frac{\epsilon_f B_f - \epsilon_b B_b}{\epsilon_f + \epsilon_b} \tag{4c}$$

where $\tilde{r}$ is the reflection coefficient, s is the fraction of photons specularly reflected, B_f (or B_b) is the non-Lambertian coefficient of the front (or back) surface, and ϵ_f (or ϵ_b) is the film emissivity of the front (or back) surface.

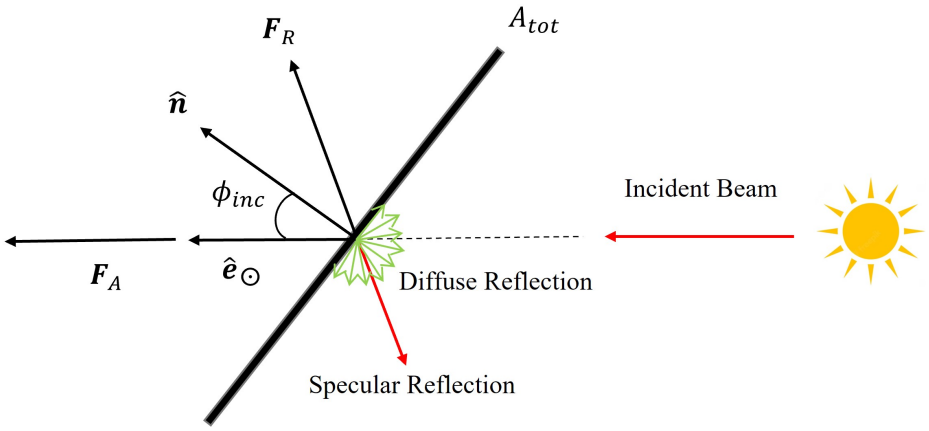

Figure 3: Solar sail illustration of sunlight reflection for a flat plate model.

In practice, the surface unit normal vector that denotes the orientation of the sail is expressed in the LVLH coordinate system as follows:

$$\hat{\boldsymbol{n}} = \cos(\alpha)\hat{\boldsymbol{r}} + \sin(\alpha)\cos(\delta)\hat{\boldsymbol{s}} + \sin(\alpha)\sin(\delta)\hat{\boldsymbol{w}} \tag{5}$$

where $\alpha \in [0, \frac{\pi}{2}]$ is the cone angle and $\delta \in [-\pi, \pi]$ is the clock angle as defined in Figure 4 in terms of the following basis vectors.

$$\hat{\boldsymbol{r}} \triangleq \frac{\boldsymbol{r}}{\| \boldsymbol{r} \|} \tag{6a}$$

$$\hat{\boldsymbol{w}} \triangleq \frac{\boldsymbol{r} \times \boldsymbol{v}}{\| \boldsymbol{r} \times \boldsymbol{v} \|} \tag{6b}$$

$$\hat{\boldsymbol{s}} \triangleq \hat{\boldsymbol{w}} \times \hat{\boldsymbol{r}} = \frac{(\boldsymbol{r} \times \boldsymbol{v}) \times \boldsymbol{r}}{\| (\boldsymbol{r} \times \boldsymbol{v}) \times \boldsymbol{r} \|} \tag{6c}$$

where $\boldsymbol{v}$ is the velocity of the spacecraft as measured by an arbitrary inertial observer.

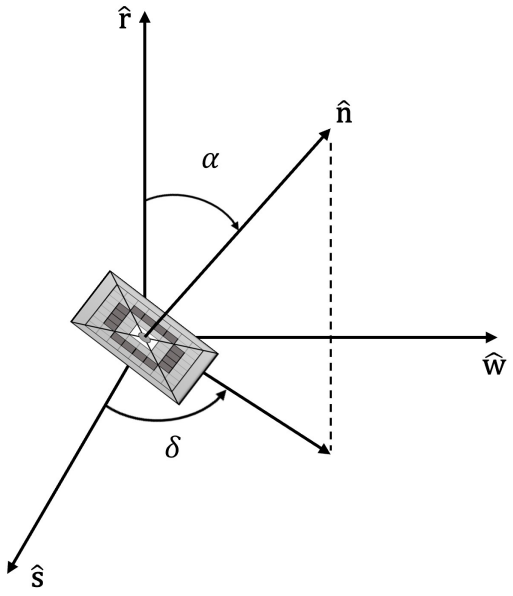

Figure 4: Sail attitude angles as expressed in the LVLH coordinate system.

2.4. Reflectivity Control Device

As explained in Caruso et al. [7], it is assumed that sunlight is diffusively reflected when the device is switched-off and specularly reflected in its on-state (Figure 5). It is assumed that only a small fraction of the total sail area A_{tot} has RCDs installed. Consequently, we defined A_s as the aluminized film area and A_{RCD}^{on} as the area covered by switched-on RCDs. In this sense, assuming the optical properties of the aluminized film area coincide with those of the switched-on RCDs, we introduce $f \in [A_s/A_{tot}, 1]$ as the reflectivity modulation ratio, defined as the fraction of the sail area in highly reflective mode.

$$f \triangleq \frac{A_s + A_{RCD}^{on}}{A_{tot}} \tag{7}$$

In practice, assuming there are sufficiently many small RCDs, f can vary accordingly from A_s/A_{tot} to 1 continuously. $f = A_s/A_{tot}$ would imply that all RCDs are switched-off. On the other hand, $f = 1$ physically denotes that all RCDs are switched-on and that the entire sail area experiences specular-dominant reflection. In this context, the reflectivity modulation ratio along

with the orientation of the sail, denoted by the surface normal vector opposite to the Sun $\hat{\boldsymbol{n}}$ (Figure 3), constitute the two control variables of this formulation to independently adjust the force magnitude and direction, respectively. The dimensionless force coefficients b_i, with $i = \{1, 2, 3\}$, in the presence of RCDs now become the following:

$$b_i = f b_i^{on} + (1 - f) b_i^{off} \tag{8}$$

In this work, the thermo-optical film properties of the NEA Scout mission are used to calculate the dimensionless force coefficients characteristic of the highly reflective mode [23]. Instead, for the switched-off RCDs, Lambertian diffusion is assumed [22] (Table 1).

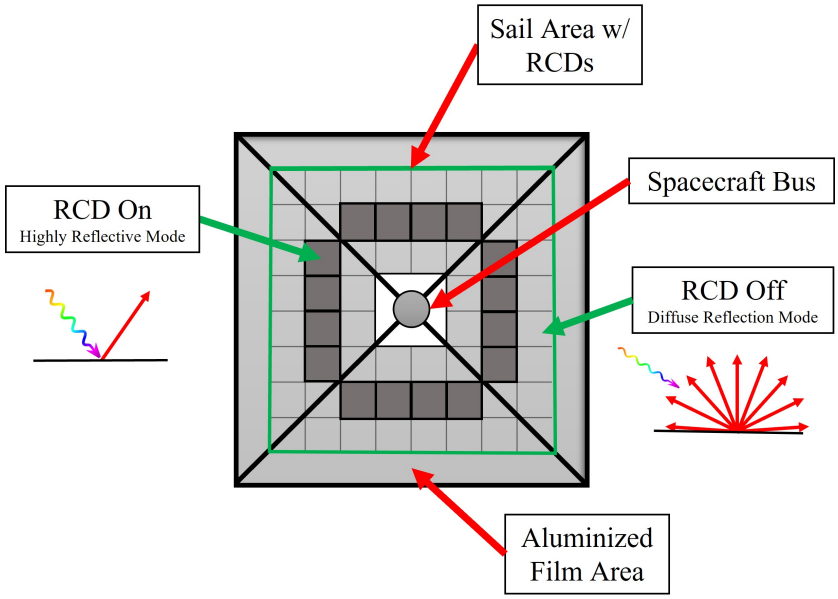

Figure 5: Solar sail schematic with reflectivity modulation technology.

Table 1: Thermo-optical film properties

Description	Symbol	Switched-On State	Switched-Off State
Reflection Coefficient	$\tilde{r}$	0.91	1
Fraction of Photons Specularly Reflected	s	0.89	0
Non-Lambertian Coefficient (Front)	B_f	0.79	2/3
Non-Lambertian Coefficient (Back)	B_b	0.67	$\sim$
Emissivity (Front)	ϵ_f	0.025	$\sim$
Emissivity (Back)	ϵ_b	0.27	$\sim$

3. Lyapunov-Based Control Design

For demonstration purposes, we consider the semimajor axis a for active control as it is well known from the literature that only one orbital element can be controlled at a time [21]. We define a positive definite Lyapunov candidate function as

$$V(\Delta a, \Delta P_{srp}) \triangleq \frac{1}{2}\Delta a^2 + \frac{1}{2}\gamma^{-1}\Delta P_{srp}^2 > 0 \tag{9}$$

where $\Delta a \triangleq a - a_d$ and $\Delta P_{srp} \triangleq P_{srp} - \hat{P}_{srp}$ are the tracking and estimation errors, respectively. a_d is the desired semimajor axis. $\gamma \in \Re$ is a positive constant control gain used to adjust the adaptation rate of the estimated parameter. By differentiating Equation (9), and substituting Equations (2a) and (3), we obtain the following expression after some algebraic manipulation.

$$\dot{V} = \frac{A_{tot}\cos(\phi_{inc})\hat{P}_{srp}\Delta a \boldsymbol{z}_a^T \tilde{\boldsymbol{u}}}{m} + \left(\frac{A_{tot}\cos(\phi_{inc})\Delta a \boldsymbol{z}_a^T \tilde{\boldsymbol{u}}}{m} - \frac{\dot{\hat{P}}_{srp}}{\gamma}\right)\Delta P_{srp} \tag{10}$$

where $\boldsymbol{z}_a^T$ is the GVE gradient of the orbital element of interest, readily available from Equation (2a), and $\tilde{\boldsymbol{u}}$ is an auxiliary control variable defined as follows to facilitate readability and the subsequent control design.

$$\boldsymbol{z}_a^T = \frac{2}{n\sqrt{1-e^2}}\begin{bmatrix} e\sin(\upsilon) & \frac{p}{r} & 0 \end{bmatrix} \tag{11}$$

$$\tilde{\boldsymbol{u}} \triangleq b_1 \hat{\boldsymbol{e}}_{\odot} + (b_2 \cos(\phi_{inc}) + b_3)\hat{\boldsymbol{n}} \tag{12}$$

From Equation (10), the update law $\dot{\hat{P}}_{srp}$ is designed to remove the estimation error dependency as well as to guarantee global exponential tracking of the unknown solar flux. Accordingly, we use an integral concurrent learning formulation suitable for the structure of the system.

$$\dot{\hat{P}}_{srp} \triangleq \frac{A_{tot} \cos(\phi_{inc}) \gamma \Delta a \boldsymbol{z}_a^T \tilde{\boldsymbol{u}}}{m} + \gamma k_{ICL} \sum_{i=1}^{N} \mathcal{Y}_i \left[a(t_i) - a(t_i - \Delta t) - \mathcal{U}_i - \mathcal{Y}_i \hat{P}_{srp} \right] \tag{13}$$

$k_{ICL} \in \Re$ is a positive constant control gain and $N \in \mathbb{Z}^+$ is the number of input-output data pairs recorded. $\mathcal{U}_i = \mathcal{U}_i(t)$ and $\mathcal{Y}_i = \mathcal{Y}_i(t)$ are defined as

$$\mathcal{Y}_i(t) \triangleq \int_{t-\Delta t}^{t} \boldsymbol{z}_a^T(\boldsymbol{q}(\tau), \tau) \boldsymbol{y}(\tau) \, \mathrm{d}\tau \tag{14}$$

$$\mathcal{U}_i(t) \triangleq \int_{t-\Delta t}^{t} \boldsymbol{z}_a^T(\boldsymbol{q}(\tau), \tau) \boldsymbol{a}_d(\tau) \, \mathrm{d}\tau \tag{15}$$

where $\boldsymbol{y}(t)$ is the measurable regression matrix, while $\Delta t \in \Re$ is a positive constant that represents the integration time window.

$$\boldsymbol{y}(t) \triangleq \frac{V A_{tot} \cos(\phi_{inc})}{m} \left(\frac{\mathrm{AU}}{r_{\odot}} \right)^2 [b_1 \hat{\boldsymbol{e}}_{\odot} + (b_2 \cos(\phi_{inc}) + b_3)\hat{\boldsymbol{n}}] \tag{16}$$

The concurrent learning term in Equation (13) represents saved data. $\mathcal{Y}_i(t)$ is the integral term that solely considers solar radiation pressure input, while $\mathcal{U}_i(t)$ accounts for other orbital perturbations. For accurate solar flux estimation, high-precision algorithms of the most dominant gravitational perturbations are required when applicable.

The update law in Equation (13) can be rewritten in an equivalent analysis form. This form of the update law suggests that if sufficient input-to-output data are recorded, $\sum \mathcal{Y}_i^2$ will be positive definite.

$$\dot{\hat{P}}_{srp} = \frac{A_{tot} \cos(\phi_{inc}) \gamma \Delta a \boldsymbol{z}_a^T \tilde{\boldsymbol{u}}}{m} + \gamma k_{ICL} \sum_{i=1}^{N} \mathcal{Y}_i^2 \Delta P_{srp} \tag{17}$$

To obtain this form of the update law, we integrate the spacecraft equations of motion that consider the time rate of change of the semimajor axis, given by Equation (2a), for the time window $[t - \Delta t, t]$ as follows.

$$\int_{t-\Delta t}^{t} \dot{a}(\tau)\, \mathrm{d}\tau = \int_{t-\Delta t}^{t} P_{srp} \boldsymbol{z}_a^T(\tau) \boldsymbol{y}(\tau)\, \mathrm{d}\tau + \int_{t-\Delta t}^{t} \boldsymbol{z}_a^T(\tau) \boldsymbol{a}_d(\tau)\, \mathrm{d}\tau \tag{18}$$

In this sense, we obtain the following relationship that relates the SRP coefficient to the measurable semimajor axis, noting that $P_{srp} = \hat{P}_{srp} + \Delta P_{srp}$ as defined previously.

$$a(t) - a(t - \Delta t) = \mathcal{Y}(t)(\hat{P}_{srp} + \Delta P_{srp}) + \mathcal{U}(t) \tag{19}$$

If we assume that the system is sufficiently excited over a finite duration of time $T \in \Re$ such that

$$\sum_{i=1}^{N} \mathcal{Y}_i^2 \geqslant \bar{\lambda} \quad \forall\, t \geqslant T \tag{20}$$

then global exponential tracking of the estimated parameters is guaranteed by Theorem 4.10 in the work of Khalil [24, 25]. Here, $\bar{\lambda} \in \Re^+$ is an user-defined threshold.

The following control law is designed for the unit normal vector denoting the spacecraft attitude to guarantee global asymptotic tracking to the desired value of the semimajor axis.

$$\hat{\boldsymbol{n}} = -\frac{m(\boldsymbol{z}_a^T \boldsymbol{z}_a)^{-1} \boldsymbol{z}_a k \Delta a}{\hat{P}_{srp} A_{tot}} \tag{21}$$

where $k \in \Re$ is a positive constant control gain designed to constrain the surface normal vector to be unitary. Notice that the solar radiation pressure force exerted on the spacecraft acts in the opposite direction of the Sun. Thus, we restrict $\phi_{inc} \in [-\frac{\pi}{2}, \frac{\pi}{2}]$. As part of the control logic, when the required orientation gives rise to an unattainable configuration, the surface normal vector is aligned perpendicular to the Sun $\left(\phi_{inc} = \frac{\pi}{2}\right)$ such that the solar radiation pressure acceleration is zero.

Given the control law in Equation (21) and the update law in Equation (17), the Lyapunov function time derivative becomes the following:

$$\dot{V} = -k \cos^2(\phi_{inc}) \Delta a^2 - k_{ICL} \sum_{i=1}^{N} \mathcal{Y}_i^2 \Delta P_{srp}^2 \tag{22}$$

The term $b_1 \hat{\boldsymbol{e}}_{\odot}$ within the auxiliary control input $\tilde{\boldsymbol{u}}$ is neglected owing to the assumption of an ideal solar sail model. This is done to simplify the analysis and ensure a feasible solution. Furthermore, as $\sum \mathcal{Y}_i^2$ is positive definite $\forall$ $t > 0$, $\dot{V}$ is upper bounded in the sense that

$$\dot{V} \leqslant -k \cos^2(\phi_{inc}) \Delta a^2 \leqslant 0 \tag{23}$$

Consequently, by invoking Barbalat's Lemma while assuming bounded eccentricity, we prove global asymptotic tracking of the semimajor axis for any value of the reflectivity modulation ratio. The control law for the reflectivity modulation ratio is adopted from Reference [7] to counteract the variation in the estimated solar flux using RCDs. In short, the required sail's cone angle and reflectivity modulation ratio are obtained using standard numerical schemes to match a desired reference trajectory assuming the clock angle equals its reference value.

3.1. Extension to Earth-Mars Transfer Orbit

As long as the Lyapunov function time derivative results in a negative semi-definite term, the preceding design and stability proof is guaranteed regardless of the control law chosen to dictate the attitude of the sail. For instance, consider a logarithmic spiral reference trajectory for an interplanetary Earth-Mars mission [1] . Here, the spacecraft attitude is fixed relative to the LVLH reference frame as the cone angle (α) is constant and the clock angle (δ) is zero.

$$\hat{\boldsymbol{n}} = \begin{bmatrix} \cos\alpha & \sin\alpha & 0 \end{bmatrix}^T \tag{24}$$

In this sense, considering Equation (9) as a valid scalar positive definite Lyapunov candidate function and the update law given by Equation (17), analogously to the geostationary debris removal case, the Lyapunov function time derivative is upper bounded while estimation of the solar flux is guaranteed.

$$\dot{V} \leqslant \frac{A_{tot}\cos\left(\phi_{inc}\right)\hat{P}_{srp}\Delta a \boldsymbol{z}_a^T \tilde{\boldsymbol{u}}}{m} \tag{25}$$

Here, Δa is a negative scalar value as the spacecraft is increasing its semimajor axis from a lower (Earth) to a higher (Mars) orbit . The inner product $\boldsymbol{z}_a^T \tilde{\boldsymbol{u}}$ is expanded to point out the contribution of each term.

$$\begin{aligned} \boldsymbol{z}_a^T \tilde{\boldsymbol{u}} = \frac{2e\sin\left(v\right)}{n\sqrt{1-e^2}}\left(b_1 + b_2\cos^2\left(\alpha\right) + b_3\cos\left(\alpha\right)\right) + \\ \frac{2p}{nr\sqrt{1-e^2}}\left(b_2\cos\left(\alpha\right)\sin\left(\alpha\right) + b_3\sin\left(\alpha\right)\right) \end{aligned} \tag{26}$$

As the eccentricity is relatively small compared to the ratio of the semilatus rectum of the orbit to its radius, the first term in Equation (26) is neglected. As a result, the Lyapunov time derivative is proven to be negative definite throughout the entire interplanetary maneuver. As it is commonly done in the literature, the excess velocity is neglected and only the interplanetary arc is considered [1].

$$\dot{V} \leqslant -\frac{A_{tot}\cos(\phi_{inc}) \mid \Delta a \mid \boldsymbol{z}_a^T \hat{P}_{srp}}{m} \left[\frac{2p}{nr\sqrt{1-e^2}}(b_2\cos(\alpha)\sin(\alpha) + b_3\sin(\alpha))\right] \quad (27)$$

4. Numerical Simulations and Discussion

In this section, numerical simulations for two sample missions are considered to test the control formulation and estimation performance: (1) a geostationary debris removal case and (2) an Earth-Mars interplanetary transfer orbit. Results are compared to trajectories with no estimation to illustrate the need to account for the actual solar flux.

4.1. Geostationary Debris Removal Mission

For demonstration purposes, a Lyapunov-based adaptive control along with integral concurrent learning is simulated in *Matlab* for a geostationary solar sail spacecraft. It is desired to increase its semimajor axis by 377 km while keeping its eccentricity bellow 0.003. This is an example of a geostationary debris removal application using solar sails in accordance with the *IADC* Space Debris Mitigation Guidelines [26]. The solar sail to consider features a mass of 1050 kg and a total surface area of 800 m^2. It is assumed that 20% of the sail area has RCDs installed. The unknown solar flux was initialized to 1500 W/m^2. In reality, the true value of the SRP coefficient was adopted as $P_{srp} = 1367/c$ W/m^2, where c is the speed of light. The disturbing accelerations include the Earth's oblateness captured by the second zonal and tesseral harmonics in addition to solar and lunar gravity to simulate the gravitational effect of neighboring celestial bodies [21, 27]. The control gains were selected as $\gamma = 10^{-20}$ and $k_{ICL} = 10^{10}$, while $\bar{\lambda}$ was set to 1×10^{-3}. The reference trajectory given by Equation (21) was integrated simultaneously with the state vector of the spacecraft. At each time step, the required cone angle and reflectivity modulation ratio were obtained using the current estimated solar flux giving a reference value of $P_{srp}^{ref} = 1375/c$ W/m^2. The algorithm adopted from Reference [7] was employed assuming a reference reflectivity modulation ratio of $\bar{f} = 0.9$. The same reference values were used for the interplanetary transfer orbit introduced in the next section.

The same adaptive control formulation discussed in this paper was also considered for the eccentricity control of the spacecraft after the first phase of the maneuver was completed (*i.e.*, the semimajor axis control phase). As shown in Figure 6 and 8, the Lyapunov-based adaptive control law tracks the desired reference for both orbital elements one at a time within 220 days. Additionally, as a means to illustrate the benefit of estimating the solar flux using integral concurrent learning, results are compared to trajectories with no ICL estimation (*i.e.*, $k_{ICL} = 0$). As expected, as time progresses, the deviation of the trajectory without estimation becomes more predominant relative to its reference. For instance, Figure 7 and Figure 9 show the residual steady state error in the semimajor axis and eccentricity for all cases considered in this study, respectively. The mean error in the semimajor axis and eccentricity of the orbit relative to its reference trajectory for $k_{ICL} = 10^{10}$ is obtained as 1.6 km and 5.8×10^{-5}, respectively. On the other hand, the mean errors for the trajectory without ICL estimation ($k_{ICL} = 0$) is computed as 3.5 km and 9.6×10^{-5} for the semimajor axis and eccentricity, correspondingly. A more significant deviation from the reference trajectory is observed for the next case in which we consider an Earth-Mars transfer orbit.

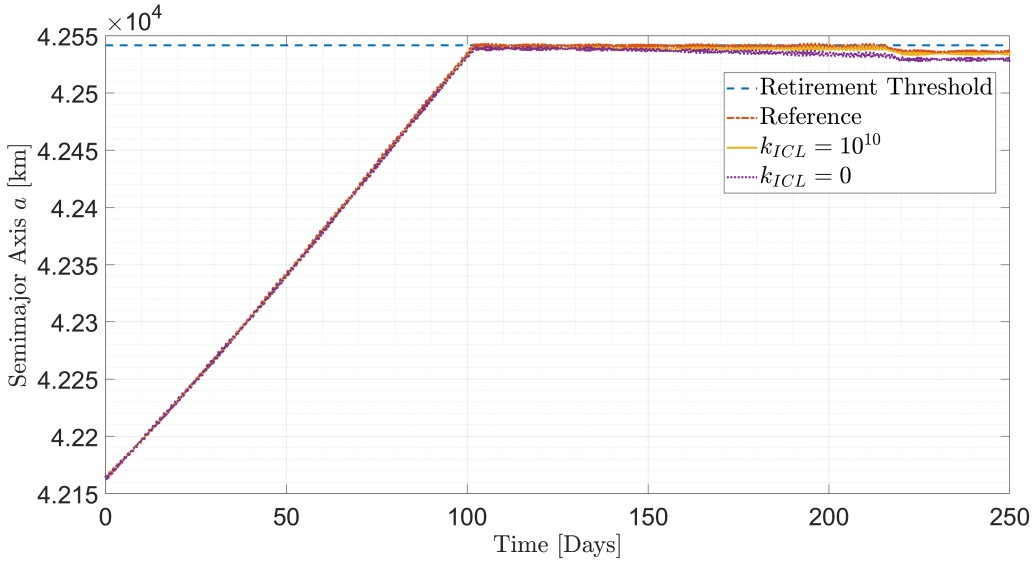

Figure 6: Semimajor axis for a GEO debris removal mission.

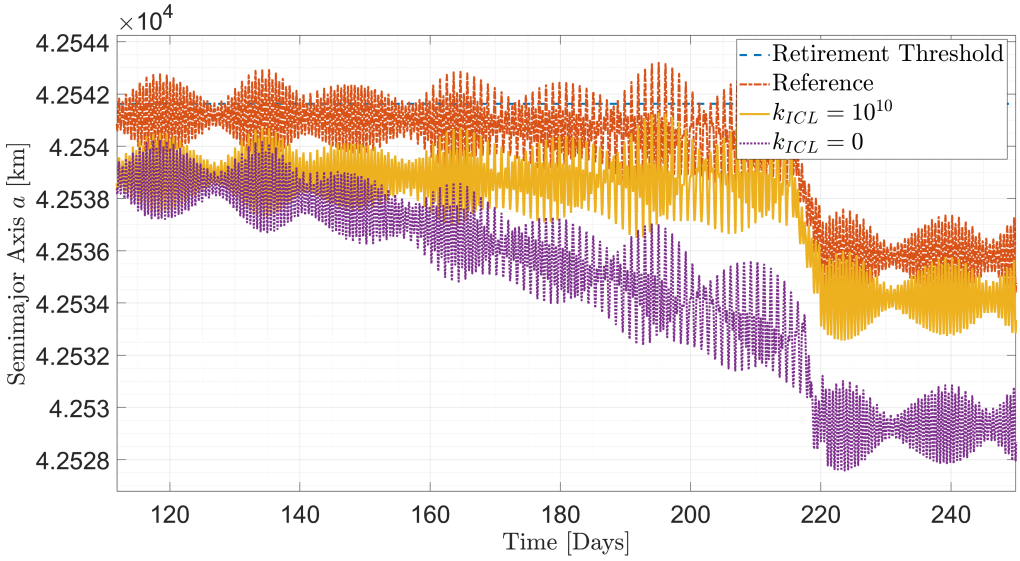

Figure 7: Semimajor axis steady state response for a GEO debris removal mission.

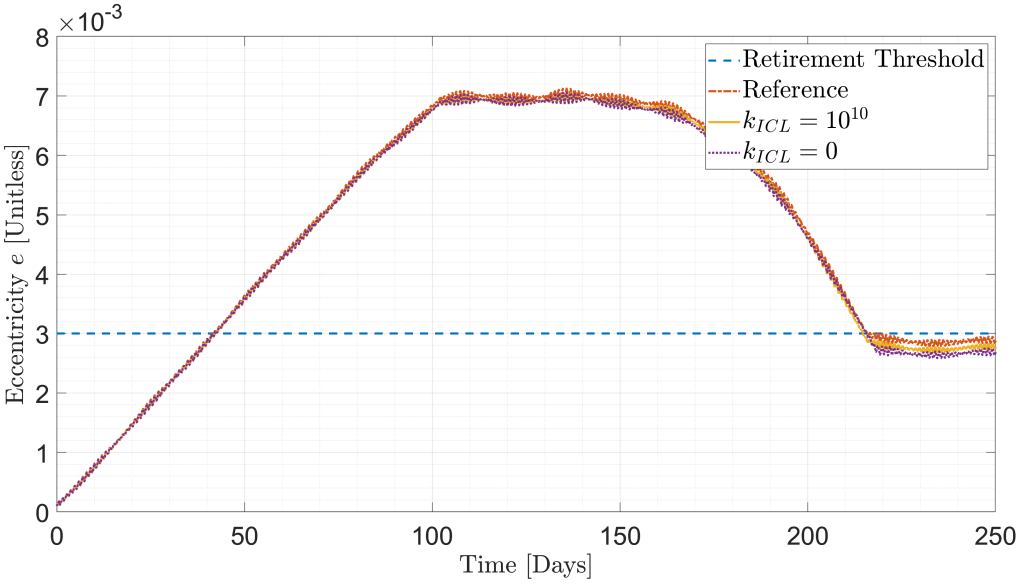

Figure 8: Eccentricity for a GEO debris removal mission.

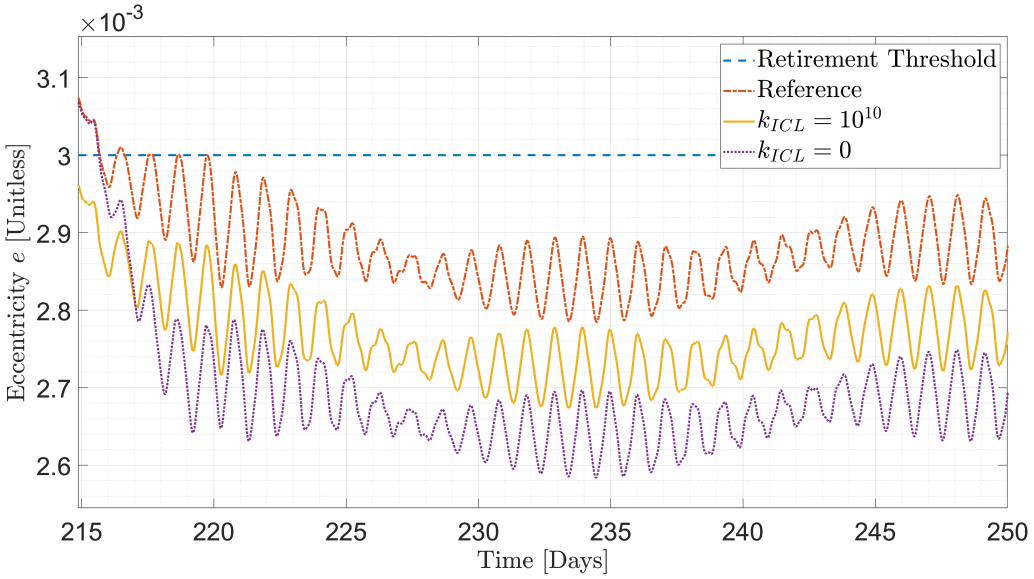

Figure 9: Eccentricity steady state response for a GEO debris removal mission.

As illustrated in Figure 10, the estimated parameter converges to its true value in about 1 day. The residual steady state estimation error is recorded as 0.27 W/m^2. This indicates that the proposed ICL formulation used to estimate the solar flux accurately approximates its actual value even for an uneducated initial guess as it is 1500 W/m^2. Moreover, over the full length of the mission, the mean estimation error is computed as 0.25 W/m^2 or equivalently 0.02%. It is important to note that better estimation was observed with smaller time steps within the simulation code to integrate the state vector. Figure 11 shows the constantly increasing behavior of $\sum \mathcal{Y}_i^2$ during the first phase of the maneuver. This indicates that the ICL terms giving by Equations (14) and (15) integrate sufficiently rich data to accurately estimate the unknown solar flux.

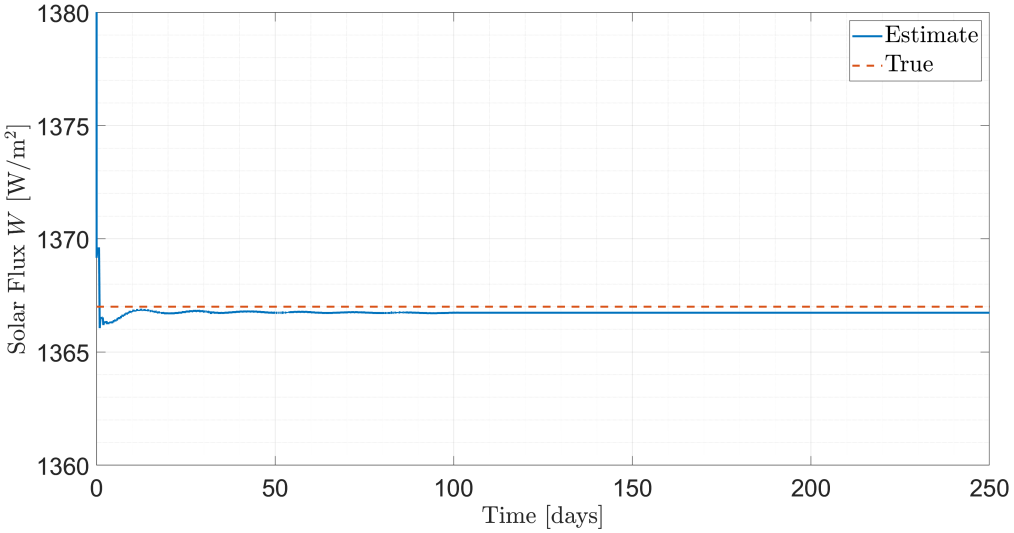

Figure 10: Solar flux estimation for GEO debris removal mission.

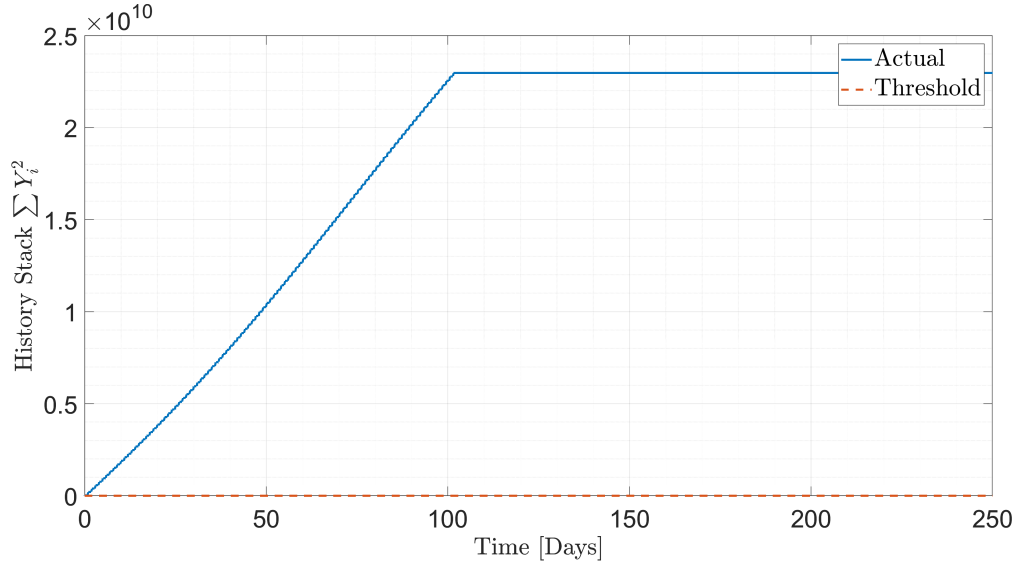

Figure 11: Minimum Eigenvalue for GEO debris removal mission.

4.2. Application to Earth-Mars Transfer Orbit

The proposed estimation technique is tested with an additional application mission to better illustrate the need to account for the unknown solar flux, the Lyapunov-based update law derived in this paper is used to estimate the solar flux given a logarithmic spiral trajectory in which the reference cone angle is considered to be $\alpha_{ref} = 35.17^{\circ}$. This value of the cone angle was obtained following the optimal control problem in Reference [1] for an ideal solar sail to minimize flight time. An ephemeris-free interplanetary transfer orbit from Earth to Mars is illustrated as a means to show the benefit of estimating the solar flux. Here, the modified equinoctial orbital elements were used to describe the spacecraft state vector for numerical integration of the equations of motion. To avoid propagation of error within the simulation, the estimates' adaptation rate was set to zero after 70 days in simulation time. Similarly to the geostationary debris removal mission, the unknown solar flux was initialized to 1500 W/m^2. The true value of the SRP coefficient was simulated as $P_{srp} = 1367/\text{c}$ W/m^2. The control gains were selected as $\gamma = 10^{-40}$ and $k_{ICL} = 10^{20}$. The solar sail to consider features the same area-to-mass ratio as of the NEA Scout $A_{tot}/m = 6.07$ m^2/kg. It was assumed that 20% of the sail area has RCDs installed.

Figure 12 shows the logarithmic spiral trajectory with ICL estimation ($k_{ICL} = 10^{30}$) and with no adaptation ($k_{ICL} = 0$) compared to a reference. A closer view by Figure 13 points out the deviation of the trajectories considered in this study. This confirms that given a wrong guess of the solar flux, the solar sail can significantly deviate from its reference. The mean tracking error is reported as 0.26 AU. Figure 14 shows the ICL estimation of the unknown parameter. Here, the steady state error is reported as 0.63 W/m^2 or equivalently 0.05%. The estimated solar flux converges to its true value within 15 days. The convergence criteria was set to 2 W/m^2. This clearly indicates that the suggested adaptive control law used to estimate the solar flux accurately approximates its actual value.

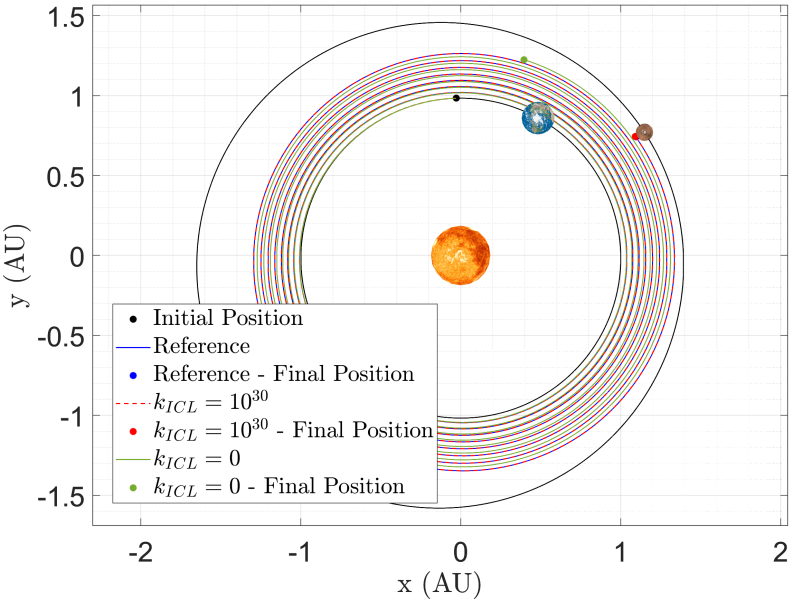

Figure 12: Earth-Mars transfer orbit.

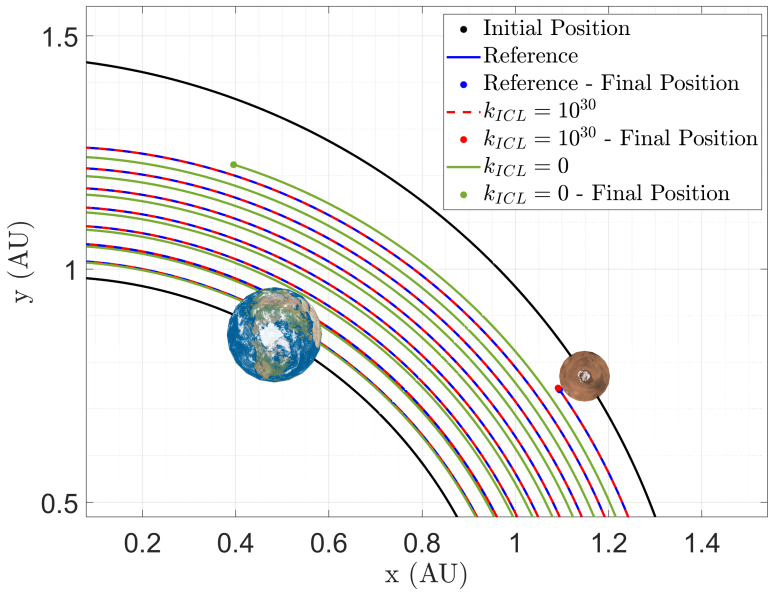

Figure 13: Earth-Mars transfer orbit at final target.

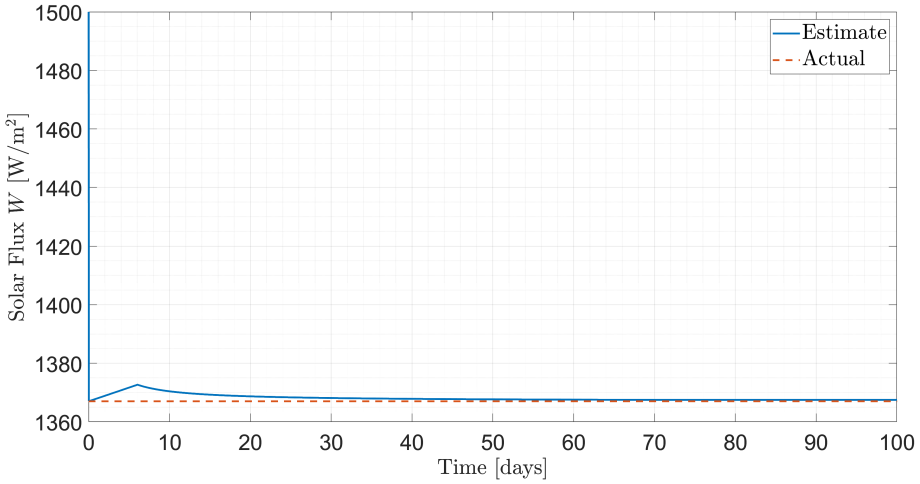

Figure 14: Solar flux estimation for Earth-Mars transfer orbit.

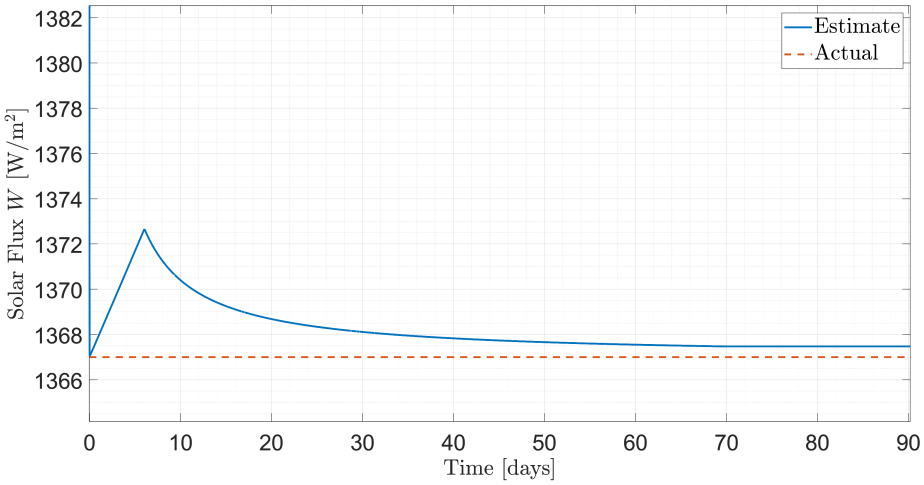

Figure 15: Close view solar flux estimation for Earth-Mars transfer orbit.

5. Conclusions and Future Work

Motivated by the desire to increase robustness and improve transient performance, as well as to avoid the use of a solar flux measuring device that would only increase the mission cost and compromise control capabilities due to unreliable measurements, the proposed adaptive control formulation demonstrates the benefit of estimating the solar flux using integral concurrent learning. Results were compared to trajectories with no estimation to illustrate the need to account for the actual solar flux. Two missions were considered: (1) a geostationary debris removal case and (2) an Earth-Mars interplanetary transfer orbit following a logarithmic spiral reference trajectory. The residual steady state estimation error was recorded as 0.27 W/m^2 for a near-Earth maneuver. Similarly, the steady state error for the Earth-Mars transfer is reported as 0.63 W/m^2, or equivalently to 0.05%. This clearly indicates that the suggested adaptive control law used to estimate the solar flux accurately approximates its actual value.

References

[1] C. R. Mclnnes, Solar Sailing: Technology, Dynamics and Mission Applications, 1^{st} ed., Springer-Verlag Berlin Heidelberg, New York, 1999.

[2] NASA, Nea scout (2022). URL: https://www.nasa.gov/content/nea-scout.

[3] NASA, Advanced composite solar sail system: Using sunlight to power deep space exploration (2021). URL: https://www.nasa.gov/directorates/spacetech/small_spacecraft/ACS3.

[4] NASA, Diffractive lightsails (2019). URL: https://www.nasa.gov/directorates/spacetech/niac/2019_Phase_I_Phase_II/Diffractive_Lightsails/.

[5] L. Niccolai, G. Mengali, A. A. Quarta, A. Caruso, Feedback control law of solar sail with variable surface reflectivity at sun-earth collinear equilibrium points, Aerospace Science and Technology 106 (2020) 183–188. doi:10.1016/j.ast.2020.106144.

[6] J. Mu, S. Gong, J. Li, Reflectivity-controlled solar sail formation flying for magnetosphere mission, Aerospace Science and Technology 30 (2013) 339–348. doi:10.1016/j.ast.2013.09.002.

[7] A. Caruso, G. Mengali, A. A. Quarta, L. Niccolai, Solar sail optimal control with solar irradiance fluctuations, Advances in Space Research 67 (2021) 2776–2783. doi:10.1016/j.asr.2020.05.037.

[8] M. Ceriotti, P. Harkness, M. McRobb, Variable-geometry solar sailing: The possibilities of the quasi-rhombic pyramid, in: Advances in Solar Sailing, Springer, 2014, pp. 899–919. doi:10.1007/978-3-642-34907-2_54.

[9] Y. Tsuda, O. Mori, R. Funase, H. Sawada, T. Yamamoto, T. Saiki, T. Endo, K. Yonekura, H. Hoshino, J. Kawaguchi, Achievement of ikaros-japanese deep space solar sail demonstration mission, Acta Astronautica 82 (2013) 183–188. doi:10.1016/j.actaastro.2012.03.032.

[10] H. Ishida, T. Chujo, O. Mori, J. Kawaguchi, Optimal design of advanced reflectivity control device for solar sails considering polarization properties of liquid crystal, in: Proceedings of the 26th International Symposium on Space Flight Dynamics, 2017. URL: https://issfd.org/ISSFD_2017/paper/ISTS-2017-d-061__ISSFD-2017-061.pdf.

[11] R. Funase, Y. Shirasawa, Y. Mimasu, O. Mori, Y. Tsuda, T. Saiki, J. Kawaguchi, On-orbit verification of fuel-free attitude control system for spinning solar sail utilizing solar radiation pressure, Advances in Space Research 48 (2011) 1740–1746. doi:10.1016/j.asr.2011.02.022.

[12] S. Gong, J. Li, Solar sail halo orbit control using reflectivity control devices, Transactions of the Japan Society for Aeronautical and Space Sciences 57 (2014) 279–288. doi:10.2322/tjsass.57.279.

[13] J. D. Biggs, A. Negri, Orbit-attitude control in a circular restricted three-body problem using distributed reflectivity devices, Journal of Guidance, Control, and Dynamics 42 (2019) 2712–2721. doi:10.2514/1.G004493.

[14] G. Vulpetti, Effect of the total solar irradiance variations on solar-sail low-eccentricity orbits, Acta Astronautica 67 (2010) 279–283. doi:10.1016/j.actaastro.2010.02.004.

[15] G. Vulpetti, Total solar irradiance fluctuation effects on sailcraft-mars rendezvous, Acta Astronautica 68 (2011) 644–650. doi:10.1016/j.actaastro.2010.01.010.

[16] F. Carlesso, A. R. Barbosa, L. E. Antunes Vieira, A. Dal Lago, et al., Solar irradiance variability monitor for the galileo solar space telescope mission: Concept and challenges, Frontiers in Physics (2022) 189–203. doi:10.3389/fphy.2022.869738.

[17] V. Sapritsky, A. Prokhorov, Absolute Primary Radiometric Thermometry, Springer International Publishing, Cham, 2020. doi:10.1007/978-3-030-57789-6_9.

[18] D. Harber, Z. Castleman, G. Drake, S. Van Dreser, N. Farber, K. Heuerman, M. Miller, J. Rutkowski, A. Sims, J. Sprunck, et al., Compact total irradiance monitor flight demonstration, in: CubeSats and SmallSats for Remote Sensing III, volume 11131, 2019, pp. 97–104. doi:10.1117/12.2531308.

[19] G. Chowdhary, Concurrent Learning for Convergence in Adaptive Control without Persistency of Excitation, Ph.D. thesis, Georgia Institute of Technology, 2010.

[20] A. Parikh, R. Kamalapurkar, W. E. Dixon, Integral concurrent learning: Adaptive control with parameter convergence using finite excitation, International Journal of Adaptive Control and Signal Processing 33 (2018) 1775–1787. doi:10.1002/acs.2945.

[21] P. Kelly, R. Bevilacqua, An optimized analytical solution for geostationary debris removal using solar sails, Acta Astronautica 162 (2019) 72–86. doi:10.1016/j.actaastro.2019.05.055.

[22] D. A. Vallado, Fundamentals of Astrodynamics and Applications, 4^{th} ed., Microcosm Press, Hawthorne, CA, 2013.

[23] A. Heaton, N. Ahmad, K. Miller, Near earth asteroid scout thrust and torque model, in: International Symposium on Solar Sailing, 2017. URL: https://ntrs.nasa.gov/citations/20170001502, paper no. M17-5721.

[24] H. Khalil, Nonlinear Systems, 3^{rd} ed., Prentice Hall, Upper Saddle River, NJ, 2002.

[25] C. Riano-Rios, R. Bevilacqua, W. E. Dixon, Differential drag-based multiple spacecraft maneuvering and on-line parameter estimation using

integral concurrent learning, Acta Astronautica 174 (2020) 189–203. doi:10.1016/j.actaastro.2020.04.059.

[26] Inter-Agency Space Debris Coordination Committee, Iadc space debris mitigation guidelines (2020). URL: https://orbitaldebris.jsc.nasa.gov/library/iadc-space-debris-guidelines-revision-2.pdf.

[27] H. Curtis, Orbital Mechanics for Engineering Students, Butterworth-Heinemann, 2013.